



Article

Synergy between Short-Range Lidar and In Situ Instruments for Determining the Atmospheric Boundary Layer Lidar Ratio

Andres Esteban Bedoya-Velázquez ¹, Romain Ceolato ^{1,*}, Gloria Titos ^{2,3}, Juan Antonio Bravo-Aranda ^{2,3}, Andrea Casans ^{2,3}, Diego Patrón ^{2,3}, Sol Fernández-Carvelo ^{2,3}, Juan Luis Guerrero-Rascado ^{2,3} and Lucas Alados-Arboledas ^{2,3}

¹ ONERA, The French Aerospace Lab, Université de Toulouse, FR 31055 Toulouse, France; andres.bedoya@onera.fr

² Department of Applied Physics, Sciences Faculty, University of Granada, 18071 Granada, Spain; gtitos@ugr.es (G.T.); jabravo@ugr.es (J.A.B.-A.); andreacasans@ugr.es (A.C.); dpatron@ugr.es (D.P.); solfcarvelo@ugr.es (S.F.-C.); rascado@ugr.es (J.L.G.-R.); alados@ugr.es (L.A.-A.)

³ Andalusian Institute for Earth System Research, IISTA-CEAMA, University of Granada, 18006 Granada, Spain

* Correspondence: romain.ceolato@onera.fr

Abstract: Short-range elastic backscatter lidar (SR-EBL) systems are remote sensing instruments for studying low atmospheric boundary layer processes. This work presents a field campaign oriented to filling the gap between the near-surface aerosol processes regarding aerosol radiative properties and connecting them with the atmospheric boundary layer (ABL), centering attention on the residual layer and the ABL transition periods. A Colibri Aerosol Lidar (CAL) instrument, based on the short-range lidar with high spatio-temporal resolution, was used for the first time in the ACTRIS AGORA facility (Andalusian Global Observatory of the Atmosphere) in Granada (Spain). This study showed the possibility of combining lidar and in situ measurements in the lowermost 150 m. The results address, on the one hand, the characterization of the short-range lidar for developing a method to find the calibration constant of the system and to correct the incomplete overlap to further data exploitation. On the other hand, relevant radiative properties such as the temporal series of the aerosol lidar ratio and extinction coefficient were quantified. The campaign was divided in three different periods based on the vehicular emission peak in the early mornings, namely, before, during, and after the emission peak. For before and after the emission peak data classification, aerosol properties presented closer values; however, large variability was obtained after the emission peak reaching the maximum values of extinction and a lidar ratio up to 51.5 ± 11.9 (Mm)⁻¹ and 36.0 ± 10.5 sr, respectively. During the emission peaks, the values reached for extinction and lidar ratio were up to 136.8 ± 26.5 (Mm)⁻¹ and 119.0 ± 22.7 sr, respectively.

Keywords: short-range lidar; lidar ratio; ABL take-off



Citation: Bedoya-Velázquez, A.E.; Ceolato, R.; Titos, G.; Bravo-Aranda, J.A.; Casans, A.; Patrón, D.; Fernández-Carvelo, S.; Guerrero-Rascado, J.L.; Alados-Arboledas, L. Synergy between Short-Range Lidar and In Situ Instruments for Determining the Atmospheric Boundary Layer Lidar Ratio. *Remote Sens.* **2024**, *16*, 1583. <https://doi.org/10.3390/rs16091583>

Academic Editor: Mark Bourassa

Received: 13 March 2024

Revised: 16 April 2024

Accepted: 23 April 2024

Published: 29 April 2024



Copyright: © 2024 by the authors. Licensee MDPI, Basel, Switzerland. This article is an open access article distributed under the terms and conditions of the Creative Commons Attribution (CC BY) license (<https://creativecommons.org/licenses/by/4.0/>).

1. Introduction

The atmospheric aerosol's relevant role in the atmosphere, particularly in the first hundreds of meters, attracts the attention of the atmospheric scientific community since it is where most human activity occurs [1,2]. Anthropogenic emissions have an impact on the biosphere and atmosphere, causing changes in the characteristics of the atmospheric boundary layer (ABL) such as height, wind, temperature, moisture, precipitation cycles, cloud formation, and air quality [3,4]. Due to still significant uncertainties regarding the spatio-temporal evolution of the near-surface ABL processes, instead of using single-system operations, most efforts have been oriented toward the synergies between different techniques such as in situ and remote sensing [5–7]. Notably, the use of remote sensors sped up in the last two decades [8,9]. For techniques such as meteorological sounding and satellite vertically resolved observations, even if they have good vertical resolution, their scarce temporal resolution and horizontal coverage inhibit their use for long-term

studies. Additionally, some satellite observations have continuous problems related to signal blocking due to cloud presence [9,10].

The Atmospheric Light Detection And Ranging (lidar) technique is underpinned as a possible tool for filling this gap since it can be used to perform measurements of aerosol radiative properties in relatively near real time (up to two samples per second) with spatial resolutions of about tens of meters [11–14]. Aerosol lidar instruments are powerful systems used to perform atmospheric measurements due to their high sensitivity to aerosol characterization, as well as their precise location ability, vertical profiling, and long measurement ranges. Lidar systems can penetrate clouds, which makes them ideal for continuous monitoring with multi-wavelength capabilities, enabling discrimination between different aerosol types based on their spectral signatures. However, recent studies have demonstrated the necessity to improve lidar's spatial and temporal resolution together with additional capabilities such as its depolarization and multi-spectral configurations [15–17] to better understand the processes that link the ABL processes and transitions (e.g., from stable to unstable conditions). Technically, lowering the blind zone is one of the main concerns related to far-range lidar since it depends on the optical configuration of the systems. In this regard, lots of studies have been conducted not only for the overlap determination [18–21], but also for lowering the full overlap height through the coupling of telescopes in the far range and the near range. The blind zone makes far-range lidars lose the capability of connecting near-surface atmospheric processes in upper atmospheric levels. Still, when considering all the efforts made in Europe through research infrastructures such as ACTRIS (www.actris.eu (accessed on 8 April 2024)) or the European Cooperation in Science and Technology actions (COST actions, www.cost.eu (accessed on 8 April 2024)), there are still significant uncertainties around this topic. ACTRIS requirements set a full overlap at 200 m, so there is an existing gap between 0 and 200 m. There are in situ instruments that can be used to explore this range based on punctual measurements of aerosol radiative and microphysical properties, and they are typically placed on high towers [22,23]; however, these instruments lack the vertical information with high spatial resolution that remote sensors can provide.

The increasing interest in characterizing low atmospheric processes linked with near-surface aerosol dynamics suggests that short-range elastic backscatter lidar should be further developed in the upcoming years. Currently, the majority of the studies involving short-range aerosol lidars have been conducted on horizontal measurements that are used to characterize nearby aerosol

sources [24–27] or the use of lidar with scanning capabilities [28] to characterize aerosol sources within the first 2 km of the atmosphere. In this work, we aimed to explore the ABL transitions/dynamics using short-range lidar

in synergy with in situ instrumentation to investigate how these transitions/dynamics influence aerosol radiative properties, centering our attention on the emission peaks measured during the field campaign.

The remainder of this manuscript is organized as follows. The campaign and instrument descriptions are found in Section 2, while the methodology is described in Section 3, focusing on the short-range lidar overlap estimation and the calibration procedures. In Section 4, the results are addressed and in Section 5 discussion can be found. Lastly, the main conclusions are presented.

2. Field Campaign and Instrumentation

2.1. Lidar LOW-Height Profiling Campaign (LiLOW)

The Lidar LOW-height profiling campaign (LiLOW) was performed at the AGORA Observatory of the Andalusian Institute for Earth System Research (IISTA) (Granada, Spain) from 9 to 12 May 2023 (see Figure 1). It aimed to (i) test a proof of concept of short-range elastic backscatter lidar (Colibri Aerosol Lidar) for vertical measurements on well-characterized emission sources, (ii) conduct inter-comparisons

of remote and in situ instruments in retrieving aerosol radiative properties within the urban ABL, and (iii) explore new synergistic combinations of instruments to improve the characterization of the low ABL aerosol properties.

AGORA Observatory is located in the city of Granada (37.160°N, 3.580°W, 680 m a.s.l) in southern Spain. Granada is a medium-sized city with a population of around 468,000 inhabitants, in 2023. The climate is typically Mediterranean with continental influence, characterized by cold winters, dry and hot summers, and a large diurnal temperature amplitude [29]. Due to its location in a valley surrounded by mountains, Granada has a well-characterized mountain-valley wind regime with up-valley winds from the NW and W during the day, and down-valley winds from the SE and E during the night and early morning [30]. The topography of the area, together with its climate, favors temperature inversions and low wind dispersion, promoting the accumulation of pollutants near the surface [31]. The main local aerosol sources are road traffic and biomass burning from agricultural waste removal practices in the outskirts of the city of Granada [32]. In addition to local sources, due to its geographical location, Granada is influenced by natural dust episodes from North Africa [33–35]. A detailed description of the different aerosols affecting Granada can be seen in [36].



Figure 1. Deployment of the instruments at the AGORA Observatory, Granada (Spain), during the LiLOW campaign. The lidar and the in situ station are operated from the same buildings with a spatial separation between the in situ inlet and lidar output window of <10 m.

The relevant physical quantities measured by each system are listed in Table 1, where it can be inferred that all data temporal resolutions were degraded to that of the instrument that presented the lowest temporal resolution for the calculations in this study.

Table 1. List of the instruments used along the campaign together with the main magnitude measured. σ_{sca} and σ_{abs} refer to the scattering and absorption coefficients, n refers to the total aerosol concentration, and RCS is the lidar range-corrected signal.

LiLOW Campaign Instrumentation					
Instrument	Property	Units	Wvl (nm)	Time Res. (s)	Spatial Res. (m)
Nephelometer	σ_{sca}	(Mm) ⁻¹	532 *	60	N/A
Aethalometer	σ_{abs}	(Mm) ⁻¹	532 **	60	N/A
SMPS	n	cm ⁻³	N/A	300	N/A
Colibri Aerosol Lidar (CAL-100)	RCS	Vm ²	532	60	0.6

* Angström exponents at 450/550 were used for the extrapolation at 532 nm. ** Angström exponents at 520/590 were used for the extrapolation at 532 nm.

2.2. Remote-Sensing Instrument: Colibri Aerosol Lidar (CAL)

Colibri Aerosol Lidar (CAL) is an instrument based on the Short-Range Elastic Backscatter Lidar (SR-EBL) technique. They are designed to measure aerosol properties close to the instrument by reducing the blind zone to less than 2 m in a bi-static and multi-axis configuration, allowing the dynamic range to change to several hundred meters. These instruments use a fast short-pulse laser source and ultrafast optical sensors and electronics to acquire the lidar signal, resulting in its high spatial resolution of 10 cm along the line of sight and high temporal resolution of up to 1 profile per millisecond. A description of the physical principles and operation can be found in [17,27,37], and the CAL-100 specifications are shown in Table 2.

Table 2. Main specifications of the Colibri Aerosol Lidar (CAL-100).

Laser	Wavelength	532 nm
	Pulse duration	<2 ns
	Pulse repetition rate	1.0 kHz
	Pulse energy	20 μ J
	Beam divergence	1.8 mrad (1/e)
	Beam diameter	2 mm (1/e)
	Bi-static angle	1–5 mrad
Receiver	Type	Cassegrain
	Effective diameter	90 mm
	Focal length	500 mm
	F-number	6.3
Sensor	Type	PMT
	Bandwidth	0.8 GHz
	Active area	200 mm ²

A proper calibration of the CAL instrument is essential to retrieve aerosol radiative and microphysical properties. Calibration can be decomposed into (i) geometric calibration, which is necessary for determining the overlap function of the lidar, especially in the short range, and (ii) radiometric calibration, which is required for retrieving the attenuated backscatter profiles and for using dedicated inverse methods that do not require any knowledge of the boundary conditions or reference zone [17,27].

2.3. In Situ Instruments

Air sampling for all the in situ instruments was obtained from the top of a stainless steel tube, 20 cm in diameter and 5 m in length [38,39]. The inlet was located about 15 m above the ground. Inside the tube, there were several stainless steel pipes driving the sampling air to the different instruments. Each one of the stainless pipes extracted the appropriate flow for each instrument. Different diameters for the pipes were selected to optimize the efficiency of the system [40].

The aerosol particle light scattering (σ_{sca}) and backscattering (σ_{back}) coefficients were measured at three wavelengths (450, 550, and 700 nm) using an integrating nephelometer (TSI 3563, Shoreview, MN, USA). This instrument draws in ambient air at a flow rate of 15 lpm, illuminates the sample with a halogen lamp, and measures scattered light at a time resolution of 1 min. The calibration of the nephelometer was carried out periodically every three months using CO₂ and filtered air. Non-idealities due to truncation errors were corrected according to [41]. For 5 min of averaging time, the detection limits for the total scattering coefficients were 0.44, 0.17, and 0.26 (Mm)⁻¹ for 450, 550, and 700 nm, respectively [42]. For backscattering, the detection limits were 0.29, 0.11, and 0.21 (Mm)⁻¹ for 450, 550, and 700 nm, respectively.

The aerosol light absorption coefficient, σ_{abs} , was measured with a Multi-Angle Absorption Photometer (MAAP, model 5012, Thermo, Norristown, PA, USA) at 637 nm [43]. The MAAP results are based on simultaneous measurements of radiation transmitted through and reflected from a particle-loaded filter at two detection angles [44]. The determination of the absorption coefficient of the filter-deposited aerosol used a radiative transfer code and explicitly included a treatment of scattering effects from the filter matrix and the light-scattering aerosol component. The two reflectivity measurements were used to correct the multiple scattering processes of the deposited particles and the filter matrix. A detailed description of the method is provided in [44]. The MAAP draws in the ambient air at a constant flow rate of 16.7 lpm and provides 1 min values. The detection limit of the MAAP instrument is lower than 0.6 Mm⁻¹ over a 2 min integration. The total method uncertainty for the particle light-absorption coefficient inferred from the MAAP measurements was around 12 % [44].

In addition to the absorption coefficient measurement performed with the MAAP, an Aethalometer AE33 (Aerosol d.o.o., Ljubljana, Slovenia) was used to estimate the black carbon mass concentration and absorption coefficients at seven wavelengths (370, 470, 520, 590, 660, 880, and 950 nm). This instrument is also based on the filter technique [45], and it was corrected by retrieving the calibration value through a comparison with the MAAP measurements [46]. The calibration value of 1.9 was obtained for the measurement period analyzed in this study.

The sub-micron particle number size distribution (PNSD, Singapore) in the diameter range 10–500 nm was monitored with a 5 min temporal resolution using a Scanning Mobility Particle Sizer (SMPS; TSI 3938) composed of an electrostatic classifier (TSI 3082) and a Condensation Particle Counter (CPC; TSI 3772). Aerosol and sheath flow rates of 1.0 and 5.0 lpm, respectively, were used. The integration of these size distributions resulted in the total aerosol number concentration. The quality of the SMPS measurements was assured by frequently checking the flow rates, monitoring the relative humidity (RH), and performing 203 nm Polystyrene Latex particle (PSL) calibration. Following the calibration procedures, the uncertainty in the measured particle size distribution was within 10% and 20% for the size ranges of 20–200 nm and 200–800 nm, respectively [47].

3. Methodology

This work combined in situ and remote sensing instruments, intending to fill the gap in the first hundreds of meters of the atmosphere. To achieve this goal, a unique configuration was proposed to validate the radiative products obtained from a non-commercial short-range lidar system co-located next to an in situ station that measures aerosol radiative and microphysical properties. Figure 2 shows the campaign's data flow and data analysis methodology. The derivations of the calibration constant and overlap function are in Section 4 based on a lidar signal inter-comparison with in situ measurements, namely, the lidar range-corrected signal (RCS) and the $\alpha_{in-situ}$. The RCS pre-processing involved background correction, bin and zero suppression, range correction, and maximum signal limit estimation through a signal-to-noise ratio (SNR) calculation, setting the maximum range of exploitable signals to up to 150 m (SNR > 3). In Section 3.2, the iterative method

of minimization used to derive the aerosol backscattering coefficient from the attenuated backscattering coefficient is detailed.

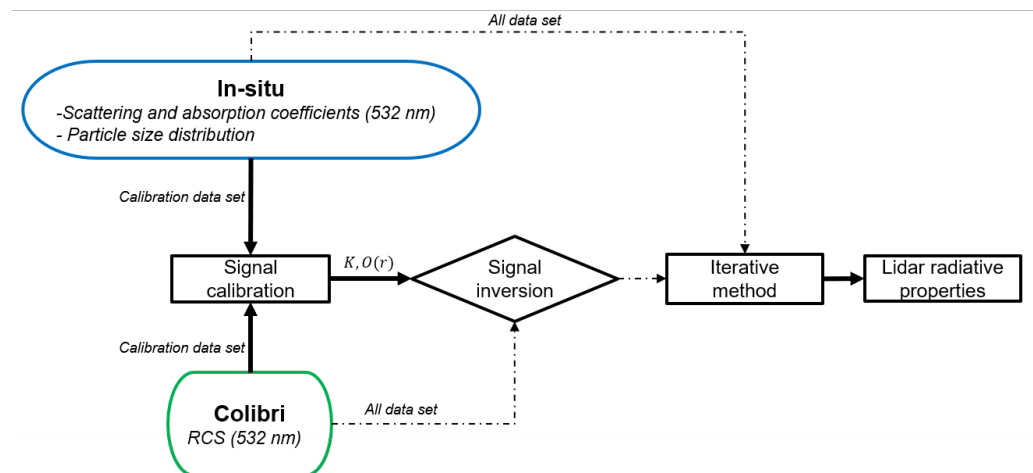


Figure 2. Block diagram of the methodology for data processing, calibration, and inversion combining short-range and in situ instruments co-located at AGORA facility during LiLOW campaign.

3.1. Theoretical Approach: Lidar Equation

The lidar equation is a radiative transfer equation that involves the interaction between aerosols and molecules with radiation in the atmosphere, resulting in a measurable physical signal $S(r,t)$. Equation (1) presents the monochromatic elastic lidar equation (wavelength dependence is omitted).

$$S(r,t) \cdot r^2 \equiv \text{RCS}(r,t) = K(t) \cdot O(r,t) \cdot \beta(r,t) \cdot \exp \left[-2 \int_0^r \alpha(r',t) dr' \right] \quad (1)$$

In Equation (1), the square of the range is already used in the left side of the equation to define the RCS. $O(r)$ is the overlap function, which refers to the signal detection probability (due to the lidar configuration's geometry). $O(r,t)$ combines all geometric effects of the transmission (laser) and receiver systems' fields of view. Typically, its value is zero near the lidar system, and it reaches unity when the laser beam is completely imaged onto the detector, and this is known as the full overlap height (FOH). $O(r,t)$ remains near the unity for ideal mono-static-coaxial or mono-static-bi-axial lidar systems; however, for bi-static lidars, the alignment plays a crucial role once the unity is reached. For far-range lidars, the unity can be assured for long distances. In contrast, due to optic limitations and user configuration needs, the overlap for short-range lidars can decrease rapidly after reaching the FOH. $K(t)$ is the lidar constant that involves all efficiency terms from detection subsystems. Substantial variations in $O(r,t)$ and $K(t)$ might be seen when geometrical modifications such as re-alignments are performed in the lidar system. In particular, temporal variations in $O(r,t)$ and $K(t)$ are linked with the aerosol load increase in the atmosphere or under abrupt temperature changes. Lastly, $\beta(r,t)$ and $\alpha(r,t)$ are the volume backscatter and extinction coefficients related with the nature of light–matter interactions.

Due to the ill-posed nature of the lidar problem, to retrieve the radiative properties from Equation (1), an extra relationship might be established between $\alpha(r)$ and $\beta(r)$. This relationship is the so-called lidar ratio, which is an intensive property that has the following form [37]:

$$\text{LR} = \frac{\alpha(r)}{\beta(r)} \quad (2)$$

For most elastic lidar data processing chains, (i) constant values of lidar LR are assumed; typically, values between 50 and 60 sr at 532 nm are often used since they include a

wide range of aerosol types such as continental pollution [48,49]. In addition, (ii) classic backward or forward inversion schemes are applied to retrieve aerosol radiative properties [50–53].

In this study, a different version of the forward Fernald inversion was applied to the short-range lidar measurements, due to the lack of boundary conditions such as a clean zone of the atmosphere in the far range. This method is also referred to as the radiometric forward Fernald inversion method [17,27] because it only requires the knowledge of the lidar constant, without knowing any boundary conditions.

3.2. Lidar Calibration and Overlap Correction

The attenuated backscatter β_{att} was retrieved by applying the overlap correction and a detailed calibration constant procedures. During the calibration period, the following assumptions were considered: (i) there were no-aerosol sporadic emissions and (ii) the atmosphere was considered homogeneous within the range of interest. To fulfill the first assumption, we used the time series of several in situ measurements, namely, Nephelometer, MAAP and SMPS measurements, to track the scattering and absorption coefficients, as well as a sub-micron size distribution together with the lidar profiles. At the same time, the hypothesis of a homogeneous atmosphere was fulfilled since most of the selected calibration periods were in the early mornings, where no-aerosol stratification was seen from the lidar signal. Additionally, an averaging of the lidar RCS signals was performed for different layers (i.e., 0 to 10 m, 10 to 20 m, 20 to 50 m, and 50 m to the end) to monitor the temporal correlation with the in situ measurements.

During this calibration period, the goal was to find the radiometric calibration constant K that would allow us to retrieve β_{att} and then apply the inversion method to obtain the α_a profiles, hereafter $\alpha_{Colibri}$. The modified form of the two-component forward Klett–Fernald method developed in [27] was used, and it is briefly introduced below:

$$\beta(r) = \beta_a(r) + \beta_m(r) = \frac{V(r)}{1 - 2 LR_a \int_{FOH}^{R_{top}} V(R) dR}. \quad (3)$$

The integration limits are set from the R_{top} , which is nothing else but the full overlap height (FOH) until R_{top} , which is the maximum range where the lidar signal presents a good signal-to-noise ratio. In this approach, the form of $\beta_{att}(r)$ is as follows:

$$\beta_{att}(r) = \beta(r) \exp \left[-2 \int_{R_{base}}^{R_{top}} LR_a \beta(R) dR \right] \exp \left[-2 \int_{R_{base}}^{R_{top}} (LR_m - LR_a) \beta_m(R) dR \right]. \quad (4)$$

where β_m is the molecular backscattering calculated based on theory and scaled to the altitude of the station. Thus, the form of $V(r)$ is

$$V(r) = \beta_{att}(r) \exp \left[2 \int_{R_{base}}^{R_{top}} (LR_m - LR_a) \beta_m(R) dR \right]. \quad (5)$$

in units of $(m \cdot sr)^{-1}$. To solve Equation (3), the LR and $\beta_{att}(r)$ are needed. Thus, LR and K will be constrained by the α differences between the in situ and Colibri measurements. The aim was to permute both quantities in an iterative procedure, where at each iteration, a β_a profile is obtained. Finally, the absolute mean bias error was used as the metric to minimize the problem as follows:

$$\min_{t_{cal} \in t} |\alpha_{Colibri}(t_{cal}) - \alpha_{in-situ}(t_{cal})| \quad (6)$$

where

$$\alpha_{Colibri}(t_{cal}) = \left\langle \sum_{i=1}^{len(perm)} f(RCS(r, t_{cal}), LR_a^i, R_{top}, K^i) \cdot LR_a^i \right\rangle_{R_{base}}^{R_{top}} \quad (7)$$

The function f inside the summation is the radiometric forward Fernald method ran for the number of permutations selected in the optimization. Once calibration is performed, $O(r)$ is estimated from Equation (1) as follows:

$$O(r) = \frac{\beta_{att}(r)}{(\alpha(r)/LR_a) \cdot \exp\left[-2 \int_0^R \alpha(R) dR\right]} \quad (8)$$

Due to the high temporal resolution of CAL-100 instrument, the calibration periods contain several profiles used to calculate the overlap. Thanks to assumptions considered for selecting the calibration periods, the resulting mean $O(r,t)$ is representative of the whole campaign, allowing us to consider the overlap as only range dependent hereafter. To minimize the effect of the signal oscillations when $O(r)$ is applied on Equation (1), an analytic function—poly fit-like—was obtained from the mean $O(r)$ to apply it systematically for signal inversion calculations.

4. Results

4.1. Measurements Time Series Analysis

Figure 3 shows the time series of $\alpha_{in-situ}$, σ_{abs} , and the total aerosol number concentration (n). At the top of the panel, in black, the Colibri mean RCS values from the FOH (32.4 m) until 150 m are presented. To link the spatio-temporal measurements from the lidar with the in situ ground-based measurements, averaging was conducted over the following five atmospheric columns in meters: [0–10], [10–20], [20–50], [50–100], and [FOH–150]. We estimated the correlation between the RCS and the $\alpha_{in-situ}$ for each atmospheric column, obtaining the following five positive correlation coefficients (R^2): 0.6, 0.6, 0.5, 0.6, and 0.5, respectively. When considering the differences in the techniques and the temporal degradation performed on the lidar data to match the resolution of the in situ instruments, the R^2 obtained is a good indicator for evaluating the synchronicity of the near-surface and the range-dependent aerosol events. The RCS until 150 m is the measurement used hereafter for the lidar time series.

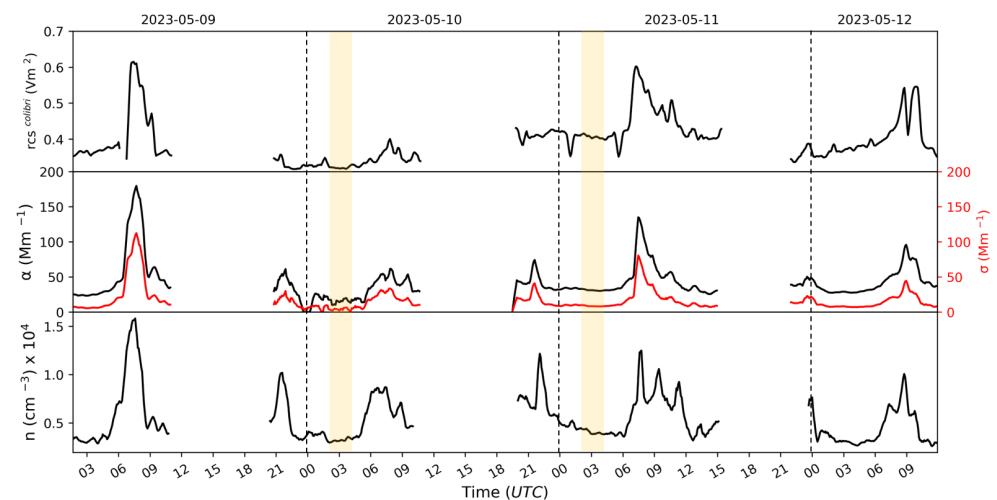


Figure 3. Time series of (top) RCS measured with Colibri (from ground to 150 m). In situ time series of σ_{abs} are presented in red and $\alpha_{in-situ}$ in black (middle), and the bottom shows the total aerosol concentration. The highlighted regions indicate the calibration time frames.

The dataset in Figure 3 exhibits two periods that we used to center the attention in this study. On the one hand, the periods where $\alpha_{in-situ}$, σ_{abs} , and n remained constant indicate the absence of aerosol particle injection and were used as calibration datasets (time slots marked in yellow). On the other hand, the slots where all variables were involved increased around 07:00 UTC. The increase was likely generated by road traffic emissions (mainly ultrafine black carbon aerosols) [54,55], allowing us to focus the study on characterizing

these emission peaks in terms of their radiative properties and their connection with the low ABL nocturnal and take-off cycles.

4.2. Calibration of the Colibri Signal

As detailed in Section 3, the calibration involves an iterative minimization calculation where the lidar constant and lidar ratio are evaluated 59,400 times to find the best values that minimize the absolute difference between $\alpha_{in-situ}$ and $\alpha_{Colibri}$. The calculation considers values of K ranging from $1 \cdot 10^4$ to $1 \cdot 10^6$ $\text{Vm}^3 \text{sr}$ with steps of $1 \cdot 10^3$ $\text{Vm}^3 \text{sr}$ and a particle lidar ratio from 30 to 150 sr with steps of 2 sr. The calibration regions were analyzed from 02:40 to 03:40 UTC since those represents an extended and stable period of the time series, indicating homogeneous media with no sudden aerosol intrusions.

In Table 3, it can be seen that the calibration constant obtained for independent measurements is quite similar, pointing out the repeatability and robustness of the calibration method. A representative calibration value of $(1.9 \pm 0.5)10^5$ $\text{Vm}^3 \text{sr}$ was used for the campaign.

Table 3. Lidar calibration constant and lidar ratio retrieved for the calibration periods.

Calibration Results			
Date	Magnitude	Units	Mean \pm Std. Dev
10 May	K	$\text{Vm}^3 \text{sr}$	$(1.9 \pm 0.2)10^5$
	LR	sr	63.1 ± 10.7
11 May	K	$\text{Vm}^3 \text{sr}$	$(1.9 \pm 0.7)10^5$
	LR	sr	67.5 ± 25.0

After the calibration, the overlap was determined from the analytical form shown in Equation (8). Figure 4 presents the results for the O(r) on 10 and 11 May in grey and green lines with its standard deviations, respectively. The mean overlap and its standard deviation are also shown in orange. When considering the mean overlap as representative for the whole campaign, the FOH was reached at 32.4 m. Lastly, as the mean O(r) profile remains with some oscillations (seen in Figure 4), a poly-fit regression was applied to use it for the overlap correction of the lidar signal for the whole campaign. Possible sources of these variations might be (i) laser instabilities due to the relatively long-time lidar operation or (ii) fast atmospheric variations that, under our high temporal sampling, can impact the O(r) mean profile mainly close to the ranges where the SNR decreases.

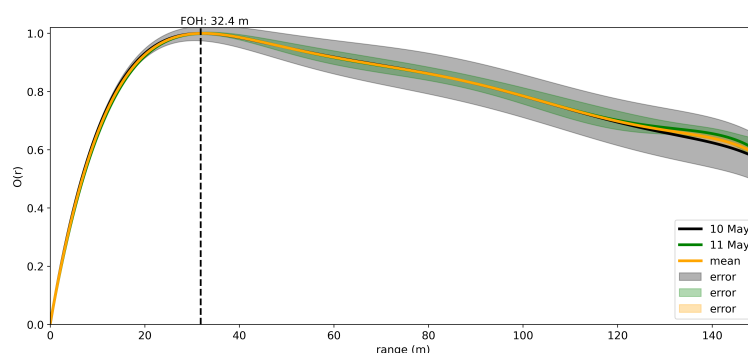


Figure 4. The mean Colibri overlap function. The straight black line is the overlap measured, while the bounded grey line is the standard deviation.

4.3. Aerosol Radiative Properties: Connection between In Situ and Colibri Measurements

A methodology based on the combination of in situ instruments and short-range lidar was proposed here to quantify the LR and study its variability as well as the α coefficient to better understand the dynamics of the low ABL. In particular, our attention is focused on the transitions from the nighttime to the startup periods. During these periods, the aerosol

radiative properties reached higher values in the early morning due to the traffic rush hours, which is likely related to the BC particle emissions.

The results are presented in Figure 5. On top, the color bar represents the LR values obtained, which are the input used to retrieve the $\alpha_{Colibri}$ profiles shown in the binary color map. From this figure, the spatio-temporal distribution of the emission peak and aerosol dispersion is seen. The $\alpha_{colibri}$ profiles show high intensity in the first 100 m during the whole campaign; however, on 9 and 11 May the intense emission peak covers the whole atmospheric column, while on 10 and 12 May, the emission peak was relatively more intense below the 100 m, exhibiting more aerosol dispersion over time.

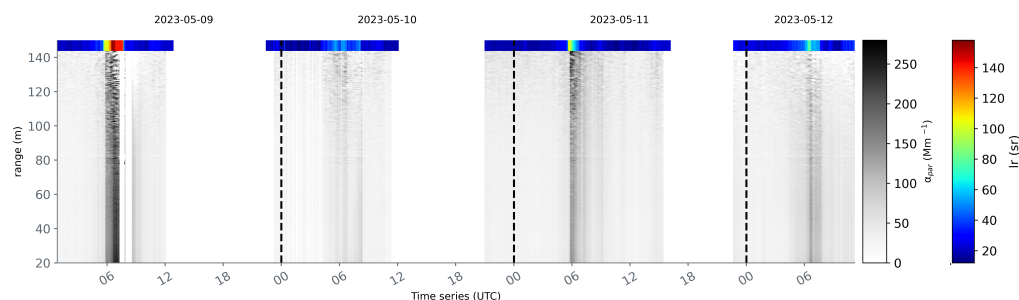


Figure 5. The binary color map of the $\alpha_{Colibri}$ retrieved using the time series of the lidar ratio found in this study as input is shown for the whole campaign. At the top of the figure, the lidar ratio time series is labeled in the color map, and each date is separated by dashed vertical lines.

Previous studies have reported values of LR up to 150 and above for freshly emitted soot particles, both experimentally [24,27] and from light-scattering models [56,57]. These results are in agreement with the results obtained during the strong traffic emission peaks measured in the campaign on 9 and 11 May, where LR values reached values up to 141.7 sr and 88.1 sr, respectively. These measurements, together with previous studies, suggest that the use of low LR values for sub-micrometric absorbing particles, such as BC, may lead to an underestimation of their radiative properties.

5. Discussion

To better understand the time of emission and dissipation of aerosols around the rush hour during the campaign, an air quality station located 1 km from the Agora Observatory was used to track the pollutant gases and particle matter (PM) concentrations over time (not shown here). As addressed in [58,59], not only do PM_{2.5} and PM₁₀ have an impact on the low ABL dynamics, but pollutant gases such as SO₂, NO_x, and others as well, which when transported from the nocturnal residual layer to the diurnal boundary layer might trigger new particle formation (NPF) processes, impacting the aerosol radiative properties and the ABL's cycle.

From the air quality station, we found that CO was predominant during the rush hours, reaching particularly high values on 9 and 10 May. NO₂ exhibited higher concentrations compared with NO and SO₂; thus, it was considered the less significant during the campaign. The PM_{2.5} mass concentration emission peaks matched with the results presented in Figure 5, with concentration levels within the acceptable values for the region.

The air quality time series helped us to determine the time duration of the emission peak and possible transport from the residual nocturnal layer, as well as qualitatively check the aerosol dissipation after the emission peak. In general, the rush hours were around 7 UTC (matching the results of previous studies in Granada [39,54,60]), with temporal lengths of 2 h. According to the air quality data, two extra periods might be analyzed, i.e., 2 h before and 2 h after the peak to determine the roles of the residual layer transport and aerosol dissipation after the emission peak. For this analysis, we assumed a low rate of vertical mixing due to turbulent movements caused by solar radiation (typically from 10 to 16 UTC [29,30]) and temporal homogeneity in the atmospheric layers.

The data were split to keep data-significance for the analysis of the aerosol radiative properties during the rush hours as follows:

- Before the emission peak, *BeP*: a two-hour mean before the start of the DeP.
- During the emission peak, *DeP*: a two-hour mean around the maximum of the emission peak.
- After the emission peak, *AeP*: a two-hour mean after the end of the DeP.

Figure 6 presents the probability density function (pdf) for each time block defined above. The LR distributions *BeP* are Gaussian-like distributions (Figure 6 on the left), with more data dispersion on 9 and 10 May. The LR distributions *DeP* (in the middle of Figure 6) exhibit less data dispersion on 9 and 12 May, while on 11 May, data distribution was broader. The LR distribution on 9 May has a particular bi-modal shape that might be linked with the higher values of the pollutant gases reached during the rush hour. As the PM data did not show any particular aerosol transport from the residual nocturnal layer to the diurnal boundary layer, the origin of these high values of radiative properties, i.e., LR and α , might be associated with the increases in CO and NO during the rush hours, which reached the highest values over the whole campaign, 400 and 50 $\mu\text{g m}^{-3}$, respectively.

After the emission peak, the data distribution is likely left-skewed with respect to the LR distributions *BeP*, pointing out that for the same time interval of 2 h, the dispersion process might play an important role, and the emission rate decreases considerably 1 h after the emission peak. During the campaign, only the air quality station acted as an indicator of the aerosol transport (*BeP*)/dispersion (*AeP*). Lastly, during the week of measurements, the concentrations of PM_{2.5} and pollutant gases *AeP* showed a monotonic decrease until reaching the typical values over the region during this hour of the day [54,60]. To better analyze the results, and according to the data distribution, the mean and standard deviation values for the LR, α_{Colibri} , and α_{Colibri} are presented in Table 4.

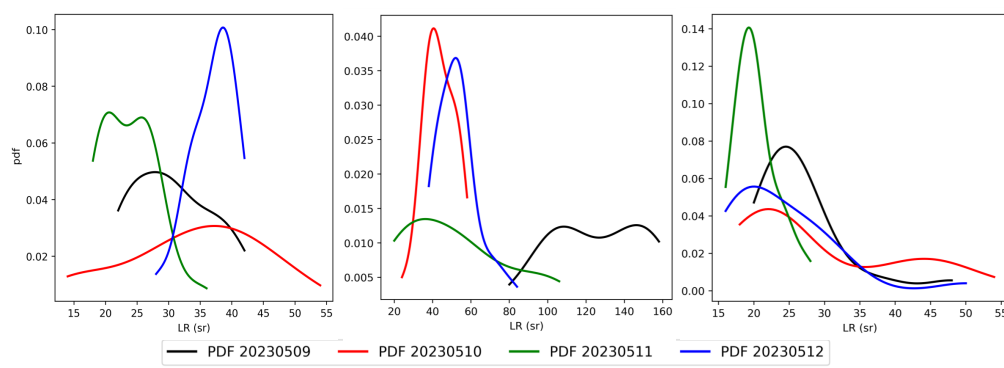


Figure 6. Probability density function of LR data for the three periods selected: *BeP* on the left, *DeP* in the middle, and *AeP* on the right. Each day is presented in a different color.

During the emission peak, the LR ranged from 96 to 141.7 sr, exhibiting a considerable increase on 9 and 11 May, which is consistent with the increase in the BC particle concentration seen with the augmentation of the σ and the total distribution number of particles (up to $1 \cdot 10^4 \text{ cm}^{-3}$). The *BeP* and *AeP* datasets point out that there were no significant differences regarding the mean values. Generally, the standard deviation values *BeP* are lower than those *AeP*, suggesting a larger data dispersion likely due to the impact of the vehicular emission peaks.

Table 4. Summary of the aerosol radiative properties in the periods of BeP, DeP, and AeP by date.

Radiative Properties					
Date	Magnitude	Units	BeP	DeP	AeP
9 May	$\alpha_{Colibri}$	(Mm) ⁻¹	38.3 ± 7.4	136.8 ± 23.5	51.4 ± 6.9
	$\alpha_{in-situ}$	(Mm) ⁻¹	53.0 ± 14.0	123.1 ± 33.0	51.9 ± 7.1
	LR	sr	32.0 ± 5.8	119.0 ± 22.7	34.0 ± 8.2
10 May	$\alpha_{Colibri}$	(Mm) ⁻¹	37.6 ± 9.2	43.7 ± 11.0	41.6 ± 10.1
	$\alpha_{in-situ}$	(Mm) ⁻¹	49.6 ± 7.0	50.0 ± 6.7	41.4 ± 7.2
	LR	sr	34.0 ± 11.7	41.0 ± 9.9	36.0 ± 10.5
11 May	$\alpha_{Colibri}$	(Mm) ⁻¹	40.6 ± 6.3	93.8 ± 20.1	48.7 ± 6.3
	$\alpha_{in-situ}$	(Mm) ⁻¹	51.4 ± 11.4	99.0 ± 21.0	49.8 ± 5.5
	LR	sr	27.0 ± 5.3	63.0 ± 25.1	22.0 ± 3.5
12 May	$\alpha_{Colibri}$	(Mm) ⁻¹	45.1 ± 4.9	76.9 ± 16.0	51.5 ± 11.9
	$\alpha_{in-situ}$	(Mm) ⁻¹	47.4 ± 4.3	74.6 ± 12.0	50.5 ± 8.5
	LR	sr	35.0 ± 4.1	61.0 ± 13.4	33.0 ± 9.9

The highest standard deviations found AeP might indicate a broader range of aerosol types presented into the air column for the following hours; thus, depending on the atmospheric conditions, this will impact the vertical mixing caused by the solar radiation and the amount of aerosols to be mixed and injected to higher layers or dispersed over the area. On the contrary, the low standard deviations found BeP indicate the well-mixing state of the aerosols before rush hours. The highest differences found between $\alpha_{Colibri}$ and $\alpha_{in-situ}$ might be associated with (i) the temporal difference of the data sampling between instruments, which impacts data variability, (ii) the origin of the data sources (in situ instruments and active remote sensing), and (iii) the noise level associated with the instruments.

6. Conclusions

A first-time campaign that involved a short-range lidar system co-located with an in situ station was deployed at the ACTRIS AGORA facility (Granada, Spain). Good correlations between the time series of range-corrected lidar signals averaged from a full overlap height of up to 150 m, the in situ extinction, the absorption coefficients, and the total aerosol concentration were found. Two periods were selected to calibrate the lidar system, assuming a homogeneous atmosphere with no sudden aerosol intrusions. Thanks to these findings, a methodology that combines lidar and in situ instruments was developed to quantify the temporal evolution of the lidar ratio and spatio-temporal evolution of the extinction coefficient during the campaign.

The data were averaged before, during, and after the emission peak to better link the temporal evolution of the aerosol radiative properties involved in this work with the atmospheric boundary layer transitions. In the classification, the first time slot refers to data before the emission peak, which considers the remaining particles within the urban residual layer during the night, while the second block contains the data during the emission peak, where new particles are emitted during the traffic rush hours, and those will be mixed with those of the residual layer. Lastly, the classification ends with a time series after the emission peak, where mixing aerosol processes and solar radiative effects start to play a major role in atmospheric dynamics. During the emission peak, the lidar ratio oscillated from 96 to 142 sr, while the lidar ratio before and after the emission peak reached values ranging from 22 to 36 sr. The results point out the relevance of including measurements of short-range lidar systems to better characterize the aerosol dynamics near the surface, which is typically the blind zone of most classical lidar systems and that connects with upper layers.

In a nutshell, this study helps us better understand the impact of near-to-surface BC emissions in the ABL evolution. Also, it demonstrates new possibilities for exploring the

aerosol dynamics near the surface, centering attention on the evolution of the residual layer and mixing processes initiated by punctual emissions and the convection of aerosol particle entrainment into the ABL.

For the near future, the following is planned:

- To continue enriching the calibration database to validate the robustness of the methodology.
- To better characterize lidar efficiency features such as detector noise, laser power, dark current, and background noises.
- To develop new campaigns involving short-range, long-range, and in situ instruments to connect the near-surface to upper atmosphere aerosol processes and their temporal evolution.

Author Contributions: A.E.B.-V. conducted the analysis and wrote the paper. R.C., J.A.B.-A., J.L.G.-R. and L.A.-A. supervised the study and provided intensive feedback on the paper. G.T., A.C. and D.P. were responsible for the in situ instruments and data. R.C. and A.E.B.-V. were responsible for the short-range lidar instrument and data. A.E.B.-V., R.C., S.F.-C. and J.A.B.-A. performed the measurements during the campaign. A.E.B.-V., S.F.-C., J.A.B.-A., D.P. and A.C. processed the data of the campaign. All authors have read and agreed to the published version of the manuscript.

Funding: This research was funded by the European research of mobility program, namely, the TNA as a part of ATMO-ACCESS research infrastructures (grant C1-A-65). This work was also founded by ONERA, The French Aerospace Lab, within the framework of the OPSIDIA and MIEL Project.

Data Availability Statement: The data presented in this study are available on request from the corresponding author.

Acknowledgments: This work is part of the Spanish national projects PID2020-120015RB-100, PID2020-117825GB-C21, and PID2020-117825GB-C22 funded by MCIN/AEI/10.13039/501100011033; Spanish project FEDER/Junta de Andalucía-Consejería de Transformación Económica, Industria, Conocimiento y Universidades/Proyecto C-EXP-366-UGR23; the University of Granada project PP2022.PP.34; the European project ATMO-ACCESS (grant agreement No. 101008004); and the Scientific Unit of Excellence: Earth System (UCE-PP2017-02). Additionally, it is part of the Spanish national project PID2020-120015RB-100 funded by MCIN/AEI/10.13039/501100011033 and received Grant PID2021-128757OB-I00 (NUCLEUS project) funded by MCIN/AEI/10.13039/501100011033/ERDFA “A way of making Europe” and this work is also a part of the project PID2022-142708NA-I00, funded by MCIN/AEI/10.13039/501100011033/FEDER,UE. Andrea Casans is funded by the Spanish ministry of research and innovation under the predoctoral program FPI (PRE2019-090827) funded by MCIN/AEI/10.13039/501100011033, FSE “El FSE invierte en tu futuro”. The authors acknowledge the National Council of Research and Development through Brazilian project 444761/2023-3. Lastly, we thank all administrative and technical support provided during the campaign by the AGORA and ONERA facilities. A special mention goes to the researchers who participated in the discussions and parallel results that were not directly part of this study but were involved in the work toward achieving the current results.

Conflicts of Interest: The corresponding author has declared that none of the authors have any conflicts of interest.

Abbreviations

The following abbreviations are used in this manuscript:

ABL	Atmospheric boundary layer;
ACTRIS	The Aerosol, Clouds and Trace Gases Research Infrastructure;
AeP	After the emission peak;
AGORA	The Andalusian Global Observatory of the Atmosphere;
BeP	Before the emission peak;
BC	Black carbon;
DeP	During the emission peak;
LiLOW	Lidar LOW-height profiling campaign;

ONERA	Office national d'études et de recherches aérospatiales;
pdf	Probability density function;
OPC	Optical particle counter;
TNA	Transnational Access

References

- Seibert, P.; Beyrich, F.; Gryning, S.E.; Joffre, S.; Rasmussen, A.; Tercier, P. Review and intercomparison of operational methods for the determination of the mixing height. *Atmos. Environ.* **2000**, *34*, 1001–1027. [[CrossRef](#)]
- Kotthaus, S.; Bravo-Aranda, J.A.; Collaud Coen, M.; Guerrero-Rascado, J.L.; Costa, M.J.; Cimini, D.; O'Connor, E.J.; Hervo, M.; Alados-Arboledas, L.; Jiménez-Portaz, M.; et al. Atmospheric boundary layer height from ground-based remote sensing: A review of capabilities and limitations. *Atmos. Meas. Tech.* **2023**, *16*, 433–479. [[CrossRef](#)]
- Garratt, J. Review: The atmospheric boundary layer. *Earth-Sci. Rev.* **1994**, *37*, 89–134. [[CrossRef](#)]
- Stull, R.B. *An Introduction to Boundary Layer Meteorology*; Springer Science & Business Media: Berlin, Germany, 1988; Volume 13.
- Altstädter, B.; Platis, A.; Wehner, B.; Scholtz, A.; Wildmann, N.; Hermann, M.; Käthner, R.; Baars, H.; Bange, J.; Lampert, A. ALADINA—An unmanned research aircraft for observing vertical and horizontal distributions of ultrafine particles within the atmospheric boundary layer. *Atmos. Meas. Tech.* **2015**, *8*, 1627–1639. [[CrossRef](#)]
- Brooks, I.M.; Tjernström, M.; Persson, P.O.G.; Shupe, M.D.; Atkinson, R.A.; Canut, G.; Birch, C.E.; Mauritsen, T.; Sedlar, J.; Brooks, B.J. The Turbulent Structure of the Arctic Summer Boundary Layer During The Arctic Summer Cloud-Ocean Study. *J. Geophys. Res. Atmos.* **2017**, *122*, 9685–9704. [[CrossRef](#)]
- Titos, G.; Ealo, M.; Román, R.; Cazorla, A.; Sola, Y.; Dubovik, O.; Alastuey, A.; Pandolfi, M. Retrieval of aerosol properties from ceilometer and photometer measurements: Long-term evaluation with in situ data and statistical analysis at Montsec (southern Pyrenees). *Atmos. Meas. Tech.* **2019**, *12*, 3255–3267. [[CrossRef](#)]
- Illingworth, A.J.; Cimini, D.; Haefele, A.; Haeffelin, M.; Hervo, M.; Kotthaus, S.; Löhnert, U.; Martinet, P.; Mattis, I.; O'Connor, E.J.; et al. How Can Existing Ground-Based Profiling Instruments Improve European Weather Forecasts? *Bull. Am. Meteorol. Soc.* **2019**, *100*, 605–619. [[CrossRef](#)]
- Cimini, D.; Haeffelin, M.; Kotthaus, S.; Löhnert, L.; Martinet, M.; O'Connor, E.; Walden, C.; Coen, M.C.; Preissler, J. Towards the profiling of the atmospheric boundary layer at European scale—Introducing the COST Action PROBE. *Bull. Atmos. Sci. Technol.* **2020**, *1*, 23–42. [[CrossRef](#)]
- Meraner, A.; Ebel, P.; Zhu, X.X.; Schmitt, M. Cloud removal in Sentinel-2 imagery using a deep residual neural network and SAR-optical data fusion. *ISPRS J. Photogramm. Remote Sens.* **2020**, *166*, 333–346. [[CrossRef](#)]
- Kotthaus, S.; Grimmond, C.S.B. Atmospheric boundary-layer characteristics from ceilometer measurements. Part 1: A new method to track mixed layer height and classify clouds. *Q. J. R. Meteorol. Soc.* **2018**, *144*, 1525–1538. [[CrossRef](#)]
- de Arruda Moreira, G.; da Silva Lopes, F.J.; Guerrero-Rascado, J.L.; da Silva, J.J.; Arleques Gomes, A.; Landulfo, E.; Alados-Arboledas, L. Analyzing the atmospheric boundary layer using high-order moments obtained from multiwavelength lidar data: Impact of wavelength choice. *Atmos. Meas. Tech.* **2019**, *12*, 4261–4276. [[CrossRef](#)]
- Kotthaus, S.; Haeffelin, M.; Drouin, M.A.; Dupont, J.C.; Grimmond, S.; Haefele, A.; Hervo, M.; Poltera, Y.; Wiegner, M. Tailored Algorithms for the Detection of the Atmospheric Boundary Layer Height from Common Automatic Lidars and Ceilometers (ALC). *Remote Sens.* **2020**, *12*, 3259. [[CrossRef](#)]
- Vivone, G.; D'Amico, G.; Summa, D.; Lolli, S.; Amodeo, A.; Bortoli, D.; Pappalardo, G. Atmospheric boundary layer height estimation from aerosol lidar: A new approach based on morphological image processing techniques. *Atmos. Chem. Phys.* **2021**, *21*, 4249–4265. [[CrossRef](#)]
- Bravo-Aranda, J.A.; de Arruda Moreira, G.; Navas-Guzmán, F.; Granados-Muñoz, M.J.; Guerrero-Rascado, J.L.; Pozo-Vázquez, D.; Arbizu-Barrena, C.; Olmo Reyes, F.J.; Mallet, M.; Alados Arboledas, L. A new methodology for PBL height estimations based on lidar depolarization measurements: Analysis and comparison against MWR and WRF model-based results. *Atmos. Chem. Phys.* **2017**, *17*, 6839–6851. [[CrossRef](#)]
- Barlow, J.; Best, M.; Bohnenstengel, S.I.; Clark, P.; Grimmond, S.; Lean, H.; Christen, A.; Emeis, S.; Haeffelin, M.; Harman, I.N.; et al. Developing a Research Strategy to Better Understand, Observe, and Simulate Urban Atmospheric Processes at Kilometer to Subkilometer Scales. *Bull. Am. Meteorol. Soc.* **2017**, *98*, ES261–ES264. [[CrossRef](#)]
- Ceolato, R.; Bedoya-Velásquez, A.E.; Mouysset, V. Short-Range Elastic Backscatter Micro-Lidar for Quantitative Aerosol Profiling with High Range and Temporal Resolution. *Remote Sens.* **2020**, *12*, 3286. [[CrossRef](#)]
- Guerrero-Rascado, J.L.; Ao Costa, M.J.; Bortoli, D.; Silva, A.M.; Lyamani, H.; Alados-Arboledas, L. Infrared lidar overlap function: An experimental determination. *Opt. Express* **2010**, *18*, 20350–20369. [[CrossRef](#)]
- Comerón, A.; Muñoz Porcar, C.; Rodríguez-Gómez, A.; Sicard, M.; Dios, F.; Gil-Díaz, C.; dos Santos Oliveira, D.C.F.; Rocadenbosch, F. An explicit formulation for the retrieval of the overlap function in an elastic and Raman aerosol lidar. *Atmos. Meas. Tech.* **2023**, *16*, 3015–3025. [[CrossRef](#)]
- Mei, L.; Ma, T.; Zhang, Z.; Fei, R.; Liu, K.; Gong, Z.; Li, H. Experimental Calibration of the Overlap Factor for the Pulsed Atmospheric Lidar by Employing a Collocated Scheimpflug Lidar. *Remote Sens.* **2020**, *12*, 1227. [[CrossRef](#)]
- Wandinger, U.; Ansmann, A. Experimental determination of the lidar overlap profile with Raman lidar. *Appl. Opt.* **2002**, *41*, 511–514. [[CrossRef](#)] [[PubMed](#)]

22. Bedoya-Velásquez, A.E.; Titos, G.; Bravo-Aranda, J.A.; Haeffelin, M.; Favez, O.; Petit, J.E.; Casquero-Vera, J.A.; Olmo-Reyes, F.J.; Montilla-Rosero, E.; Hoyos, C.D.; et al. Long-term aerosol optical hygroscopicity study at the ACTRIS SIRTIA observatory: Synergy between ceilometer and in situ measurements. *Atmos. Chem. Phys.* **2019**, *19*, 7883–7896. [[CrossRef](#)]
23. Andreae, M.O.; Acevedo, O.C.; Araujo, A.; Artaxo, P.; Barbosa, C.G.G.; Barbosa, H.M.J.; Brito, J.; Carbone, S.; Chi, X.; Cintra, B.B.L.; et al. The Amazon Tall Tower Observatory (ATTO): Overview of pilot measurements on ecosystem ecology, meteorology, trace gases, and aerosols. *Atmos. Chem. Phys.* **2015**, *15*, 10723–10776. [[CrossRef](#)]
24. Mazzoleni, C.; Kuhns, H.D.; Moosmüller, H. Monitoring Automotive Particulate Matter Emissions with LiDAR: A Review. *Remote Sens.* **2010**, *2*, 1077–1119. [[CrossRef](#)]
25. Jin, Y.; Sugimoto, N.; Nishizawa, T.; Yoshitomi, T.; Sawada, A.; Sarae, W.; Hattori, A.; Yamasaki, Y.; Okamoto, H.; Sato, K. Measurement of water mist particle size generated by rocket launch using a two-wavelength multi-static lidar. *Appl. Opt.* **2019**, *58*, 6274–6279. [[CrossRef](#)] [[PubMed](#)]
26. Ong, P.M.; Lagrosas, N.; Shiina, T.; Kuze, H. Surface Aerosol Properties Studied Using a Near-Horizontal Lidar. *Atmosphere* **2020**, *11*, 36. [[CrossRef](#)]
27. Ceolato, R.; Bedoya-Velasquez, A.; Fossard, F.; Mouysset, V.; Paulien, L.; Lefebvre, S.; Mazzoleni, C.; Sorensen, C.; Berg, M.; Yon, J. Black carbon aerosol number and mass concentration measurements by picosecond short-range elastic backscatter lidar. *Sci. Rep.* **2022**, *12*, 761–775. [[CrossRef](#)] [[PubMed](#)]
28. Guerrero-Rascado, J.L.; da Costa, R.F.; Bedoya, A.E.; Guardani, R.; Alados-Arboledas, L.; Bastidas, Á.E.; Landulfo, E. Multispectral elastic scanning lidar for industrial flare research: Characterizing the electronic subsystem and application. *Opt. Express* **2014**, *22*, 31063–31077. [[CrossRef](#)] [[PubMed](#)]
29. Bedoya-Velásquez, A.E.; Navas-Guzmán, F.; de Arruda Moreira, G.; Román, R.; Cazorla, A.; Ortiz-Amezcuca, P.; Benavent-Oltra, J.A.; Alados-Arboledas, L.; Olmo-Reyes, F.J.; Foyo-Moreno, I.; et al. Seasonal analysis of the atmosphere during five years by using microwave radiometry over a mid-latitude site. *Atmos. Res.* **2019**, *218*, 78–89. [[CrossRef](#)]
30. Ortiz-Amezcuca, P.; Martínez-Herrera, A.; Manninen, A.J.; Pentikäinen, P.P.; O'Connor, E.J.; Guerrero-Rascado, J.L.; Alados-Arboledas, L. Wind and Turbulence Statistics in the Urban Boundary Layer over a Mountain—Valley System in Granada, Spain. *Remote Sens.* **2022**, *14*, 2321. [[CrossRef](#)]
31. Lyamani, H.; Fernández-Gálvez, J.; Pérez-Ramírez, D.; Valenzuela, A.; Antón, M.; Alados, I.; Titos, G.; Olmo, F.; Alados-Arboledas, L. Aerosol properties over two urban sites in South Spain during an extended stagnation episode in winter season. *Atmos. Environ.* **2012**, *62*, 424–432. [[CrossRef](#)]
32. Titos, G.; del Águila, A.; Cazorla, A.; Lyamani, H.; Casquero-Vera, J.; Colombi, C.; Cuccia, E.; Gianelle, V.; Močnik, G.; Alastuey, A.; et al. Spatial and temporal variability of carbonaceous aerosols: Assessing the impact of biomass burning in the urban environment. *Sci. Total Environ.* **2017**, *578*, 613–625. [[CrossRef](#)] [[PubMed](#)]
33. Lyamani, H.; Bravo Aranda, J.; Alados Arboledas, L. Informe de calidad del aire de Granada: Año 2009. In *Grupo de Física de la Atmósfera*; Universidad de Granada, Centro Andaluz del Medio Ambiente: Granada, Spain, 2010.
34. Lyamani, H.; Olmo, F.; Alcántara, A.; Alados-Arboledas, L. Atmospheric aerosols during the 2003 heat wave in southeastern Spain I: Spectral optical depth. *Atmos. Environ.* **2006**, *40*, 6453–6464. [[CrossRef](#)]
35. Valenzuela, A.; Olmo, F.; Lyamani, H.; Antón, M.; Quirantes, A.; Alados-Arboledas, L. Analysis of the columnar radiative properties retrieved during African desert dust events over Granada (2005–2010) using principal plane sky radiances and spheroids retrieval procedure. *Atmos. Res.* **2012**, *104–105*, 292–301. [[CrossRef](#)]
36. Foyo-Moreno, I.; Lozano, I.L.; Alados, I.; Guerrero-Rascado, J.L. A new method to estimate aerosol radiative forcing on photosynthetically active radiation. *Atmos. Res.* **2023**, *291*, 106819. [[CrossRef](#)]
37. Ceolato, R.; Berg, M.J. Aerosol light extinction and backscattering: A review with a lidar perspective. *J. Quant. Spectrosc. Radiat. Transf.* **2021**, *262*, 107492. [[CrossRef](#)]
38. Lyamani, H.; Olmo, F.; Alados-Arboledas, L. Light scattering and absorption properties of aerosol particles in the urban environment of Granada, Spain. *Atmos. Environ.* **2008**, *42*, 2630–2642. [[CrossRef](#)]
39. Lyamani, H.; Olmo, F.J.; Alados-Arboledas, L. Physical and optical properties of aerosols over an urban location in Spain: Seasonal and diurnal variability. *Atmos. Chem. Phys.* **2010**, *10*, 239–254. [[CrossRef](#)]
40. Willeke, K.; Baron, P.A.; Martonen, T. *Aerosol Measurement: Principles, Techniques, and Applications*; Van Nostrand Reinhold New York: New York, NY, USA, 1993; Volume 876.
41. Anderson, T.L.; Ogren, J.A. Determining Aerosol Radiative Properties Using the TSI 3563 Integrating Nephelometer. *Aerosol Sci. Technol.* **1998**, *29*, 57–69. [[CrossRef](#)]
42. Anderson, T.; Covert, D.; Marshall, S.; Laucks, M.; Charlson, R.; Waggoner, A.; Ogren, J.; Caldow, R.; Holm, R.; Quant, F.; et al. Performance Characteristics of a High-Sensitivity, Three-Wavelength, Total Scatter/Backscatter Nephelometer. *J. Atmos. Ocean. Technol.* **1996**, *13*, 967–986. [[CrossRef](#)]
43. Müller, T.; Laborde, M.; Kassell, G.; Wiedensohler, A. Design and performance of a three-wavelength LED-based total scatter and backscatter integrating nephelometer. *Atmos. Meas. Tech.* **2011**, *4*, 1291–1303. [[CrossRef](#)]
44. Petzold, A.; Schönlinner, M. Multi-angle absorption photometry—A new method for the measurement of aerosol light absorption and atmospheric black carbon. *J. Aerosol Sci.* **2004**, *35*, 421–441. [[CrossRef](#)]

45. Drinovec, L.; Močnik, G.; Zotter, P.; Prévôt, A.S.H.; Ruckstuhl, C.; Coz, E.; Rupakheti, M.; Sciare, J.; Müller, T.; Wiedensohler, A.; et al. The “dual-spot” Aethalometer: An improved measurement of aerosol black carbon with real-time loading compensation. *Atmos. Meas. Tech.* **2015**, *8*, 1965–1979. [[CrossRef](#)]
46. Yus-Díez, J.; Via, M.; Alastuey, A.; Karanasiou, A.; Minguillón, M.C.; Perez, N.; Querol, X.; Reche, C.; Ivančič, M.; Rigler, M.; et al. Absorption enhancement of black carbon particles in a Mediterranean city and countryside: Effect of particulate matter chemistry, ageing and trend analysis. *Atmos. Chem. Phys.* **2022**, *22*, 8439–8456. [[CrossRef](#)]
47. Wiedensohler, A.; Wiesner, A.; Weinhold, K.; Birmili, W.; Hermann, M.; Merkel, M.; Müller, T.; Pfeifer, S.; Schmidt, A.; Tuch, T.; et al. Mobility particle size spectrometers: Calibration procedures and measurement uncertainties. *Aerosol Sci. Technol.* **2018**, *52*, 146–164. [[CrossRef](#)]
48. Peng, L.; Yi, F.; Liu, F.; Yin, Z.; He, Y. Optical properties of aerosol and cloud particles measured by a single-line-extracted pure rotational Raman lidar. *Opt. Express* **2021**, *29*, 21947–21964. [[CrossRef](#)] [[PubMed](#)]
49. Mylonaki, M.; Giannakaki, E.; Papayannis, A.; Papanikolaou, C.A.; Komppula, M.; Nicolae, D.; Papagiannopoulos, N.; Amodeo, A.; Baars, H.; Soupiona, O. Aerosol type classification analysis using EARLINET multiwavelength and depolarization lidar observations. *Atmos. Chem. Phys.* **2021**, *21*, 2211–2227. [[CrossRef](#)]
50. Klett, J.D. Stable analytical inversion solution for processing lidar returns. *Appl. Opt.* **1981**, *20*, 211–220. [[CrossRef](#)] [[PubMed](#)]
51. Klett, J.D. Lidar inversion with variable backscatter/extinction ratios. *Appl. Opt.* **1985**, *24*, 1638–1643. [[CrossRef](#)]
52. Fernald, F.G.; Herman, B.M.; Reagan, J.A. Determination of aerosol height distributions by lidar. *J. Appl. Meteorol.* **1972**, *11*, 482–489. [[CrossRef](#)]
53. Fernald, F.G. Analysis of atmospheric lidar observations: Some comments. *Appl. Opt.* **1984**, *23*, 652–653. [[CrossRef](#)]
54. Titos, G.; Lyamani, H.; Pandolfi, M.; Alastuey, A.; Alados-Arboledas, L. Identification of fine (PM₁) and coarse (PM₁₀₋₁) sources of particulate matter in an urban environment. *Atmos. Environ.* **2014**, *89*, 593–602. [[CrossRef](#)]
55. Rejano, F.; Casquero-Vera, J.A.; Lyamani, H.; Andrews, E.; Casans, A.; Pérez-Ramírez, D.; Alados-Arboledas, L.; Titos, G.; Olmo, F.J. Impact of urban aerosols on the cloud condensation activity using a clustering model. *Sci. Total Environ.* **2023**, *858*, 159657. [[CrossRef](#)] [[PubMed](#)]
56. Paulien, L.; Ceolato, R.; Soucasse, L.; Enguehard, F.; Soufiani, A. Lidar-relevant radiative properties of soot fractal aggregate ensembles. *J. Quant. Spectrosc. Radiat. Transf.* **2020**, *241*, 106706. [[CrossRef](#)]
57. Liu, L.; Mishchenko, M.I. Spectrally dependent linear depolarization and lidar ratios for nonspherical smoke aerosols. *J. Quant. Spectrosc. Radiat. Transf.* **2020**, *248*, 106953. [[CrossRef](#)] [[PubMed](#)]
58. Casquero-Vera, J.A.; Lyamani, H.; Dada, L.; Hakala, S.; Paasonen, P.; Román, R.; Fraile, R.; Petäjä, T.; Olmo-Reyes, F.J.; Alados-Arboledas, L. New particle formation at urban and high-altitude remote sites in the south-eastern Iberian Peninsula. *Atmos. Chem. Phys.* **2020**, *20*, 14253–14271. [[CrossRef](#)]
59. Wang, Y.; Ma, Y.; Yan, C.; Yao, L.; Cai, R.; Li, S.; Lin, Z.; Zhao, X.; Yin, R.; Deng, C.; et al. Sulfur Dioxide Transported From the Residual Layer Drives Atmospheric Nucleation During Haze Periods in Beijing. *Geophys. Res. Lett.* **2023**, *50*, e2022GL100514. [[CrossRef](#)]
60. Titos, G.; Lyamani, H.; Drinovec, L.; Olmo, F.; Močnik, G.; Alados-Arboledas, L. Evaluation of the impact of transportation changes on air quality. *Atmos. Environ.* **2015**, *114*, 19–31. [[CrossRef](#)]

Disclaimer/Publisher’s Note: The statements, opinions and data contained in all publications are solely those of the individual author(s) and contributor(s) and not of MDPI and/or the editor(s). MDPI and/or the editor(s) disclaim responsibility for any injury to people or property resulting from any ideas, methods, instructions or products referred to in the content.